Topological and superconducting properties of monolayered CoN and CoP: A first-principles comparative study

Jiaqing Gao[1], Zhenyu Zhang[1,2], and Ping Cui[1,2*]

[1] *International Center for Quantum Design of Functional Materials (ICQD), Hefei National Research Center for Physical Sciences at Microscale (HFNL), University of Science and Technology of China, Hefei 230026, China;*
[2] *Hefei National Laboratory, University of Science and Technology of China, Hefei 230088, China*

Two-dimensional systems that simultaneously harbor superconductivity and nontrivial band topology may serve as appealing platforms for realizing topological superconductivity with promising applications in fault-tolerant quantum computing. Here, based on first-principles calculations, we show that monolayered CoN and CoP with the isovalent FeSe-like structure are stable in freestanding form, even though their known bulk phases have no resemblance to layering. The two systems are further revealed to display intrinsic band inversions due to crystal field splitting, and such orderings are preserved with the inclusion of spin-orbit coupling (SOC), which otherwise is able to open a curved band gap, yielding a non-zero Z_2 topological invariant in each case. Such a mechanism of topologicalization is distinctly contrasted with that identified recently for the closely related monolayers of CoX (X = As, Sb, Bi), where the SOC plays an indispensable role in causing a nontrivial band inversion. Next, we demonstrate that, by applying equi-biaxial tensile strain, the electron-phonon coupling strength in monolayered CoN can be significantly enhanced, yielding a superconducting transition temperature (T_c) up to 7-12 K for the Coulomb pseudopotential of $\mu^* = 0.2$-0.1, while the CoP monolayer shows very low T_c even under pronounced strain. Their different superconducting behaviors can be attributed to different variations in lattice softening and electronic density of states around the Fermi level upon pressuring. Our central findings enrich the understanding of different mechanisms of band inversions and topologicalization and offer platforms for achieving the coexistence of superconductivity and nontrivial band topology based on two-dimensional systems.

band topology, superconductivity, 2D materials, first-principles approaches

PACS number(s): 71.15.Mb, 73.20.At, 74.70.-b, 74.78.-w

1   Introduction

In the past few decades, two-dimensional (2D) superconductors have been investigated comprehensibly because such systems exhibit a variety of novel quantum phenomena. At a detailed materials level, tremendous advances have been made in highly crystalline 2D superconductors [1], in part

enabled by the latest developments of sophisticated fabrication approaches. Compelling examples include the emergence of superconductivity at the insulator/insulator or metal/insulator interfaces, even though none of the constituent materials is superconducting [2,3]. Ultrathin metal films grown on proper substrates have also been observed to preserve their superconductivity down to the monolayer or bilayer regime [4,5], and atomically thin band insulators can be tuned into the superconducting regime upon electric-field

gating [6,7]. Strikingly, for layered materials with weak interlayer coupling, the superconducting transition temperature (T_c) of a monolayer can be as high as its bulk counterpart or drastically enhanced over the bulk value when grown on proper substrates, as demonstrated respectively in Cu- [8] or Fe-based superconductors [9]. These developments provide material systems platforms for gaining a better understanding of unconventional superconductivity.

As one special type of unconventional superconductivity, topological superconductivity (TSC) has gained particular attention due to its promising potential for application in topological quantum computing [10]. Tremendous efforts have been devoted to searching for 2D materials harboring simultaneously superconductivity and topologically nontrivial band properties, driven by realizing TSC and Majorana zero modes in the 2D limit [11]. One route to materializing 2D TSC is to achieve an unconventionally paired superconductor, i.e., an intrinsic topological superconductor in which superconductivity and nontrivial topology arise from the same electronic states of a given system. For example, a monolayered Pb_3Bi alloy was proposed to harbor chiral *p*-wave superconductivity by taking advantage of the interplay between electron correlation and geometric phase [12]. The (nearly) flat bands in twisted or untwisted few-layer graphene with strongly enhanced electronic correlations may also provide an effective pathway toward unconventional superconductivity [13-16]. A separate and widely explored route to realizing 2D TSC is to exploit proximity effects in reciprocal space, where the superconducting bands are proximity coupled to the topological edge states, mimicking effective 2D chiral *p*-wave superconductors. Compelling examples include heavily doped MoS_2 thin films [17], monolayered FeSe [18,19], Fe(Te,Se) [20,21], gated WTe_2 monolayers [22-25], bilayered $PdTe_2$ [26], W_2N_3 [27,28], CoX (X = As, Sb, Bi) [29], and few-layered stanene films on the Bi(111) substrate [30]. Given these exciting developments, it is still highly desirable to further broaden the candidate materials for realizing 2D TSC, especially because definitive experimental detection of the corresponding topological edge or Majorana zero modes remains elusive in many cases.

In this paper, by using first-principles calculations, we predict stable monolayered CoN and CoP structures, even though none of which is a layered material in bulk form; we also carry out a comparative study of their electronic, topological, and superconducting properties. The CoN and CoP monolayers are first shown to adopt FeSe-like layered structures, which can be attributed to the isovalence nature of these systems. Next, we demonstrate that the two systems possess topologically nontrivial band properties, as revealed by the inverted band structures, Z_2 topological invariants, and robust edge states. Such a band topology is also rather robust against equi-biaxial strain. Unlike the closely related CoX (X

= As, Sb, Bi) monolayers obeying the Bernevig-Hughes-Zhang (BHZ) model [31], where the spin-orbit coupling (SOC) has been shown to induce a nontrivial band inversion [29], here the SOC just lifts the band degeneracy and opens a nontrivial curved band gap in each of the two systems, which is similar to the Kane-Mele (KM) model [32]. Finally, we show that even though either of the two freestanding monolayers possesses a low T_c, large enhancements in the electron-phonon coupling (EPC) and T_c of monolayered CoN are observed when exerting a tensile equi-biaxial strain, whereas the superconductivity of monolayered CoP is insensitive to the strain. The underlying reasons can be attributed to the differences in the electronic density of states around the Fermi level and phonon softening upon pressuring. These central findings enrich the understanding of different band-inversion and topological mechanisms and provide a promising platform for the realization of TSC in the 2D limit.

This paper is organized as follows. In sect. 2, we briefly describe the computational methods and details. The main results are presented in sect. 3. We first identify the crystal structures of monolayered CoN and CoP, with their thermodynamic and dynamic stabilities confirmed. The electronic structures and topological properties of both systems (including evolution under lattice deformation) are further discussed, together with the underlying mechanisms of topologicalization. We then investigate the superconducting properties of these two systems, and analyze the dependencies of the EPC and T_c on tensile stain. The magnetic properties are also investigated by considering four specific magnetic configurations, indicating that the CoN and CoP systems have a much weaker tendency toward developing magnetization compared with FeSe. In sect. 4, we discuss several physically realistic growth aspects of the CoN and CoP monolayers, and summarize our findings.

2   Computational details

We have employed the Vienna *Ab initio* Simulation Package (VASP) [33] for structural optimization, electronic property calculations, and *ab initio* molecular dynamics (AIMD) simulations based on density functional theory (DFT), using the projector augmented wave (PAW) method [34] and generalized gradient approximation (GGA) with Perdew-Burke-Ernzerhof (PBE) functional [35]. The kinetic energy cutoff of the plane-wave basis was chosen to be 600 eV, the electronic minimizations were performed with an energy tolerance of 10^{-8} eV, and optimized atomic structures were achieved until the residual forces on each atom were smaller than 0.001 eV/Å. A $1 \times 1 \times 1$ surface supercell and a $21 \times 21 \times 1$ *k*-point mesh for the CoN and CoP monolayers were used during structural optimization and electronic property cal-

culations. A vacuum of more than 18 Å was set to avoid spurious interactions between periodic layers. In the AIMD simulations, the canonical NVT (*N*: number of particles; *V*: volume; *T*: temperature) ensemble was adopted with Nosé-Hoover thermostat [36,37]. A $5 \times 5 \times 1$ supercell and a $3 \times 3 \times 1$ *k*-point mesh were used for both monolayers. Each time step was set to 3 fs and simulations were conducted for more than 1000 steps (3 ps) at 300 K. The Z_2 topological invariant was calculated via the Wannier charge center method [38], and the edge Green's function [39] was obtained by using the maximally localized Wannier functions [40], as implemented in the Wannier90 package [41] and WannierTools package [42].

The vibrational properties and EPC within density functional perturbation theory (DFPT) were calculated by using the EPW code [43] as implemented in the Quantum ESPRESSO package [44]. We used norm-conserving pseudo-potentials with the PBE of GGA as the exchange-correlation function [45]. For electronic charger density calculations, the kinetic energy cutoff of the plane-wave basis was chosen to be 120 Ry for both systems, and the Brillouin zone was sampled with a uniform unshifted *k*-mesh of $18 \times 18 \times 1$. The electron-phonon matrix elements were first calculated on a coarse *k*-mesh of $18 \times 18 \times 1$ in the electron Brillouin zone and a coarse *q*-mesh of $6 \times 6 \times 1$ in the phonon Brillouin zone, and then were interpolated into a finer *k*-mesh of $180 \times 180 \times 1$ and a finer *q*-mesh of $90 \times 90 \times 1$. The Dirac delta functions were replaced by Lorentzians of widths of 50 and 0.5 meV for electrons and phonons, respectively.

The superconducting transition temperature T_c was estimated based on the standard McMillan-Allen-Dynes formula [46,47]:

$$k_B T_c = \frac{\hbar \omega_{\log}}{1.2} \exp\left[-\frac{1.04(1+\lambda)}{\lambda - \mu^*(1+0.62\lambda)}\right], \tag{1}$$

where $\omega_{\log}$ is the logarithmic average of the phonon frequencies, λ is the total EPC strength, and the electron-electron effective repulsion was treated semi-empirically through the Coulomb pseudopotential μ^* with a reasonable value in the standard range of 0.1-0.2 [48]. The branch- (*v*) and momentum- (*q*) resolved EPC parameter λ_{qv} is defined as:

$$\lambda_{qv} = \frac{\gamma_{qv}}{\pi N(\varepsilon_F)\omega_{qv}^2}, \tag{2}$$

where $N(\varepsilon_F)$ is the density of states at the Fermi level, and γ_{qv} and ω_{qv} are the phonon linewidth and phonon frequency for the phonon branch *v* with the wave vector *q*, respectively. The Eliashberg function $\alpha^2F(\omega)$ is defined as:

$$\alpha^2F(\omega) = \frac{1}{2}\sum_v \frac{dq}{\Omega_{BZ}}\delta(\omega - \omega_{qv})\omega_{qv}\lambda_{qv}, \tag{3}$$

where Ω_{BZ} is the volume of the phonon Brillouin zone. The accumulative EPC $\lambda(\omega)$ can be calculated by

$$\lambda(\omega) = 2\int_0^\omega \frac{\alpha^2F(v)}{v}dv. \tag{4}$$

The total EPC λ is obtained by taking the upper bound ω to ∞ in eq. (4).

3 Results

3.1 Crystal structures and stabilities

Most known crystalline 2D systems, including superconductors, are derived from intrinsically layered materials in bulk form [49]. However, recent developments in discoveries of 2D materials also revealed that certain materials with no preference for layering in bulk phases can nevertheless be stabilized in the 2D limit [50-52], offering alternative pathways for achieving the design of 2D materials. Experimentally, such novel forms of 2D materials predicted by theory have been successfully fabricated by molecular beam epitaxy (MBE) growth techniques, such as tellurene [53-55], CuSe [56,57], CoSb [58], AlSb [59], and CuI [60]. Similar to the already reported CoX (X = As, Sb, Bi) monolayers, based on the isovalency nature with FeSe, we expect the two systems of CoN and CoP are likely to be stabilized in the FeSe-like monolayer structure as well (i.e., the PbO-type structure), even though they lack layered structures in the 3D counterparts. Indeed, as shown in Figure 1(a), the CoN (CoP) monolayer can be stabilized as a three-atomic-layer structure, where the cobalt atoms form a square lattice and the nitrogen (phosphorus) atoms are located symmetrically above and below the central squared layer of cobalt. Upon structural optimization, the calculated in-plane lattice parameter for 2D CoN (CoP) is 3.302 (3.578) Å, with the monolayer thickness of 1.814 (2.507) Å from top N to bottom N (P to P).

To further examine their thermodynamic and dynamic stabilities, AIMD simulations and phonon dispersion analysis have been carried out for each system. During the AIMD simulations, each system keeps its initial structure at 300 K as shown in Figure 1(b) and (c), indicating their thermodynamic stability. Meanwhile, the phonon spectra of the two freestanding monolayers are presented in Figure 1(d) and (e) using an electronic broadening $\sigma = 0.02$ Ry, showing that the frequencies of all phonon branches in the whole Brillouin zone are positive values, and confirming that such structures are also dynamically stable. To investigate the possibility of charge density waves (CDWs), we also calculate the phonon spectra using a smaller $\sigma = 0.01$ Ry (Figure S1 in Supporting Information), and show no imaginary frequency or even apparent softening of phonon modes, compared with the results with $\sigma = 0.02$ Ry (Figure 1(d) and (e)). These results further confirm their structural stability, and indicate that there is no tendency to CDW in the two systems.
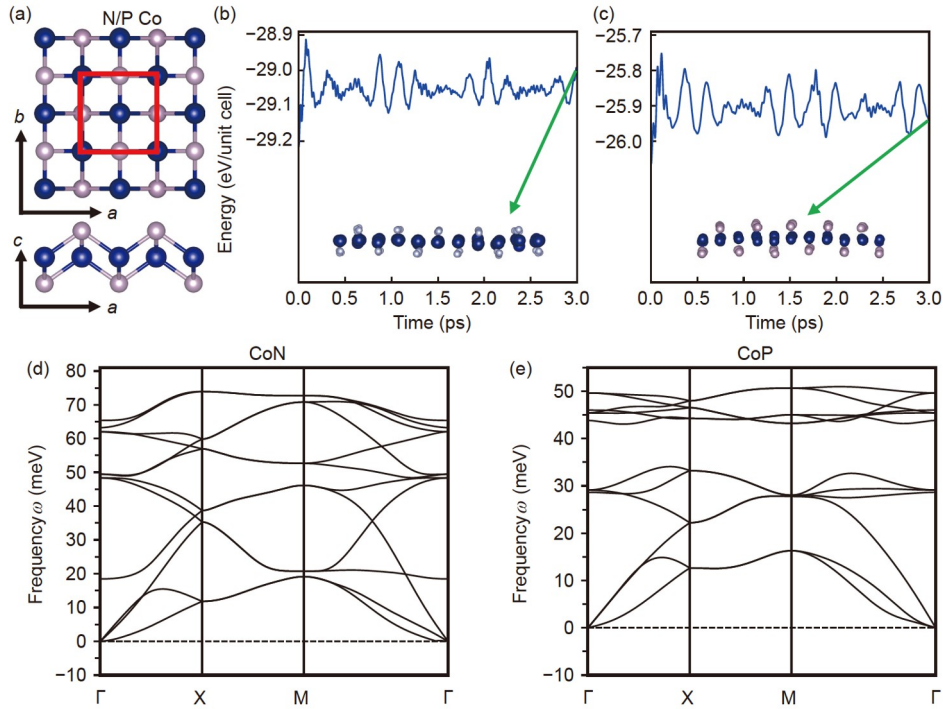
Figure 1 (Color online) (a) Top (upper panel) and side (lower panel) views of crystal structures of monolayered CoN and CoP, with the unit cell indicated in red. The blue and grey balls represent the cobalt and nitrogen (phosphorus) atoms, respectively. (b), (c) Evolutions of the total energies of monolayered CoN and CoP during AIMD simulations at 300 K and up to 3 ps. Insets display the side views of the atomic structures at the end of the simulations. (d), (e) Phonon spectra of monolayered CoN and CoP.

3.2   Electronic structures and topological properties

The band structures of the CoN and CoP monolayers with the inclusion of the SOC indicate the two systems are both metallic, as shown in Figure 2(a) and (b). In general, the topology of a system with a global gap can be determined by calculating the Z_2 topological invariant; while for a metallic system, to identify the topological properties, an effective Z_2 can still be defined by following a curved Fermi level invoking the so-called band proximity effect [11,61]. Here, we define the curved Fermi levels for both monolayers as given in Figure 2(a) and (b). It is noted that no curved Fermi level can be defined in the absence of the SOC, and the two systems are trivial in this case. Before calculating the Z_2, we analyze the band gap opening and band inversion behaviors around the curved Fermi levels, which are closely tied to the nontrivial band topology and topologicalization mechanism for the overall systems. The zoom-ins of the GGA and GGA + SOC bands near the Γ point are depicted with orbital projections in Figure 2(c) and (d). For CoN, without the SOC, the lowest conduction band (LCB) and highest valence band (HVB), which are defined according to the curved Fermi level in Figure 2(a), display a camelback shape near the Γ point in the 2D Brillouin zone (BZ). When considering the SOC, two Dirac cones centered at finite momenta along the M-Γ-X direction in the 2D BZ both open up fundamental

gaps, forming a curved band gap. In particular, around the Γ point, the HVB mainly consists of Co-d_{xz}/d_{yz} and Co-d_{xy} orbitals, and the LCB mainly consists of hybridized Co-d_{z^2} and N-p_z orbitals, revealing an intrinsic band inversion that is caused by the crystal field effect. For CoP, in the absence of the SOC, the LCB and HVB (also defined according to the curved Fermi level in Figure 2(b)) degenerate at the Γ point, only composed of the Co-d_{xz}/d_{yz} orbitals, and the rest of the LCB (namely, except the Γ point) mainly consists of the hybridized Co-d_{xz}/d_{yz} and d_{xy} orbitals, as indicated by the fatband analysis. When the SOC is included, the degeneracy at the Γ point is lifted, resulting in a finite gap. Although there is an inversion of the Co-d_{xz}/d_{yz} orbitals from the HVB to the LCB around the Γ point, the LCB and HVB at the Γ point are still composed of the Co-d_{xz}/d_{yz} orbitals, with the latter being responsible for topological properties. Therefore, the SOC only opens a band gap without leading to a band inversion at the Γ point.

To further identify the topological properties of both systems, we calculate the Z_2 topological invariant from wave functions for all occupied bands defined by the curved Fermi level. We find $Z_2 = 1$ for the CoN and CoP systems, indicating that they are both topologically nontrivial. To further highlight their topological nature, their local densities of states are calculated as shown in Figure 2(e) and (f). In the
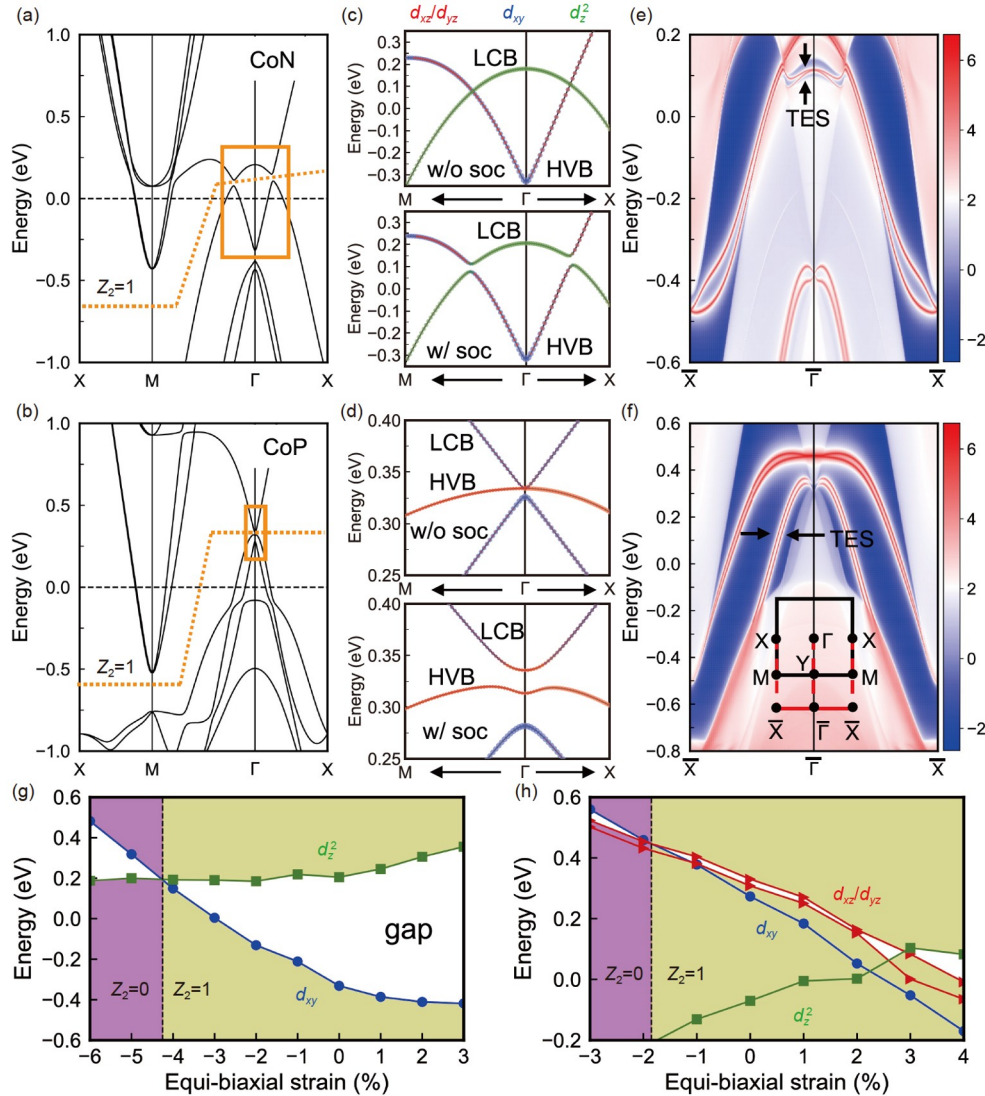
Figure 2   (Color online) (a), (b) Band structures of freestanding CoN and CoP monolayers, as calculated with the inclusion of the SOC. The orange dashed lines correspond to the curved Fermi levels. (c), (d) Zoom-in views of the orange solid boxes in (a) and (b), with orbital projections. The top and bottom panels display the results calculated without and with the SOC, respectively. The radii of the red, blue, and green dots indicate the spectral weights of different d orbitals of the Co atoms. (e), (f) Topological edge states (TESs) of monolayered CoN and CoP along the [100] edge. The warmer colors denote the higher local density of states, and the blue regions denote the bulk band gaps. The inset of (f) is the corresponding first Brillouin zone and the [100] edge. (g), (h) Energy levels of different d orbitals of the Co atoms near the curved Fermi levels for CoN and CoP at the Γ point under different equi-biaxial strains with the SOC. The Fermi levels are all set at zero.

CoN system, a pair of topologically protected edge states are clearly seen to cross at the Γ point. In the CoP system, the topological edge states connect the bulk valence and conduction bands to form a single Dirac cone at the $\overline{X}$ point in principle, but the tails of the edge states overlap with the bulk states so that the Dirac point cannot be seen. Here, the SOC just breaks the degeneracy at the Dirac cone or touching point and then opens a nontrivial curved band gap, but the SOC does not induce any band inversion between the valence and conduction bands at the time-reversal invariant momenta. Indeed, these two systems, similar to some other previously established 2D systems [62-66], already possess intrinsic band inversions even without the SOC, and in this

sense, they share a similar mechanism towards topologicalization to the KM model for graphene [32]. Furthermore, although the SOC only opens a curved band gap in CoN and CoP rather than a global gap as in graphene, the valence and conduction bands can still be defined by the curved Fermi level, and the corresponding Z_2 invariant can be calculated. Such an approach in identifying the band topology has been employed in earlier studies, for example, for the Fe(Se,Te) systems [61].

It is worthwhile to point out that the mechanism for the nontrivial band topology in CoN and CoP is distinctly different from that in the CoX (X = As, Sb, Bi) systems, where the SOC first closes the trivial band gap and then opens a

nontrivial gap, accompanied by a band inversion between the valence and conduction bands [29]. Whereas the former follows that of the KM model [32], the latter obeys the BHZ model for quantum wells [31]. Indeed, the topology in the CoX systems is the result of the delicate competition between the crystal field and SOC effects. The crystal field effect is highly related to the atomic structures including the lattice constant a and vertical distance h defined between the pnictogen atom and cobalt plane, while the SOC is mainly determined by the pnictogen atoms. Going from the freestanding CoN to CoBi monolayers, both the a and h gradually increase, leading to different orderings of the five Co-d orbital levels. The resulting LCB and HVB around the Γ point change from an initial crossover behavior (already inverted in CoN) to degenerate states (in CoP), and further to an increasing gap (with a trivial order in CoX (X = As, Sb, Bi)) in the absence of the SOC according to Figures 2 and 4 of ref. [29]. When the a and h are relatively small, the strong crystal field effect has led to the reversal of the bands; with the a and h increasing and the crystal field effect decreasing, the band inversion is absent without the SOC but is further induced by the SOC. Collectively, the full range of CoX (X = N, P, As, Sb, Bi) systems provides an ideal materials platform to contrast the different underlying mechanisms of how unusual band inversions can be developed.

Given that only the bands at the Γ point are responsible for their topological behaviors for the two systems, to further illustrate the effect of the band inversions, we present in Figure 2(g) and (h) the calculated energy levels $|d_{xz}/d_{yz}\rangle$, $|d_{xy}\rangle$, $|d_{z^2}\rangle$ near the curved Fermi levels at the Γ point for CoN and CoP under an equi-biaxial strain, in which $\varepsilon_{aa} = \varepsilon_{bb}$, where ε_{aa} and ε_{bb} are the external strains along the a and b directions, respectively. For CoN, when compressing the lattice, the $|d_{xy}\rangle$ level shifts upwards and gets closer to the $|d_{z^2}\rangle$ level, reaching a crossing between the two levels at a critical strain of around −4%. After this level crossing, the band inversion between the LCB and HVB is absent, as demonstrated by the orbital projected band structures shown in Figure S2, thereby inducing a topological phase transition from a nontrivial phase ($Z_2 = 1$) to a trivial phase ($Z_2 = 0$). Similarly, for CoP, the band inversion between the $|d_{xy}\rangle$ and $|d_{xz}/d_{yz}\rangle$ energy levels exists under the strains from −1% to +4%, as shown in Figure S3, leading to a topologically nontrivial to trivial phase transition around −2%. Here, though the $|d_{z^2}\rangle$ level moves upwards and turns above the $|d_{xz}/d_{yz}\rangle$ level under +3% and +4%, such a band inversion does not cause a topological phase transition. It is worth noting that the nontrivial topological phases of the two systems can survive during the lattice stretching, indicating their robustness against lattice deformation.

3.3 Superconducting properties

The phonon spectra with the λ_{qv} indicated by the sizes of the red circles, phonon density of states, Eliashberg functions $\alpha^2F(\omega)$, and EPC strength λ of the CoN and CoP monolayers are reported in Figure 3(a) and (b), respectively. As we can see, although the EPC strength of each system is relatively small, the λ of the CoN ($\lambda = 0.36$, $T_c = 0.5$ K, $\mu^* = 0.1$) is still much larger than that of the CoP ($\lambda = 0.23$, $T_c = 0.002$ K, $\mu^* = 0.1$). The underlying reason for such a difference is tied to the different contributions to the overall EPC strength from the low-frequency acoustic phonon branches, which account for nearly 67% of the total λ in each system. Specifically, the λ_{qv}'s of the CoN along the ΓX and ΓM directions are more prominent than that of the CoP, suggesting that the low-frequency acoustic phonon modes, which are dominated by in-plane vibrations (Figure 3(g)) interact strongly with the electronic states. This can also be reflected by the partial charge distribution around the Fermi level. As shown in Figure 3(h), the charge more noticeably pervades in the interatomic space for the CoN; accordingly, the in-plane vibrational modes are more likely to influence these electronic states, and contribute to the overall λ. Note that the SOC is not included in the electron-phonon calculations presented here. We have checked the effects of the SOC on phonon spectra, λ, and electronic density of states (DOS) in the two systems, as shown in Figure S4, and confirm that the SOC effects are negligible. Here, we also note that the McMillan-Allen-Dynes formula for calculating T_c is derived from the isotropic Migdal-Eliashberg theory. Nevertheless, according to Figure 3(a)-(d), the primary contribution to the total EPC comes from the vicinity of the Γ point, indicating the dominance of forward electron-phonon scattering (small $|q|$) to the EPC. To this extent, our systems are also largely isotropic; therefore, it is reasonable to use this formula to estimate T_c. Furthermore, the weaker screening effect for the 2D systems can be effectively compensated by the emergence of low-frequency collective excitations such as the plasmon modes [67], in essence extending the range of applicability of the McMillan-Allen-Dynes formula originally derived from the 3D cases.

Unlike bulk systems, 2D materials offer greater manipulation possibilities by applying an external strain, which can effectively tune their superconductivity [68-70]. Here, we further investigate how the equi-biaxial strain can affect the electron-phonon interaction and superconducting transition temperature T_c in the CoN and CoP systems. By invoking compressive and expansive isostatic deformations of the lattice, variations in the T_c, total EPC constant λ, logarithmic frequency ω_{log}, and electronic density of states at the Fermi energy $N(\varepsilon_F)$ for both systems are summarized in Figure 3(i).
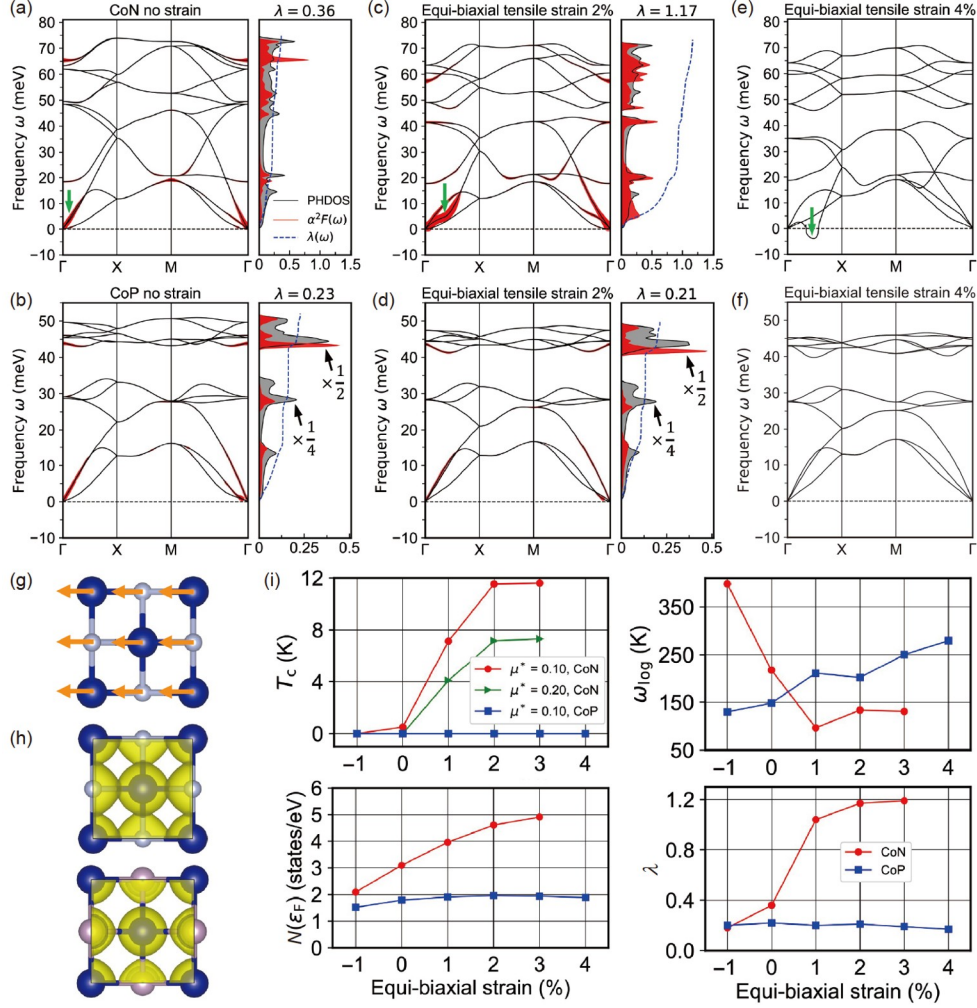
Figure 3   (Color online) Superconducting properties of the CoN monolayer under (a) no strain and (c) an equi-biaxial tensile strain of 2%. The left panels are the phonon spectra with the branch (v)- and momentum (q)-resolved EPC parameters λ_{qv} indicated by the sizes of the red circles. The right panels are the phonon density of states (PHDOS), Eliashberg function $\alpha^2F(\omega)$, and cumulative EPC strength $\lambda(\omega)$. (b), (d) Same as (a) and (c) but for the CoP monolayer. The magnitudes of PHDOS and $\alpha^2F(\omega)$ are minified by a factor of 4 and 2, respectively. (e), (f) The corresponding phonon spectra under the equi-biaxial tensile strain of 4%. (g) Schematic diagram of the acoustic mode indicated by the green arrows in (a), (c), and (e). (h) Partial charge distributions within the range of −0.02-0.02 eV around the Fermi level for the CoN (upper panel) and CoP (lower panel) monolayers. (i) Strain dependences of the superconducting transition temperature T_c, logarithmically averaged phonon frequency $\omega_{\log}$, electronic density of states at the Fermi energy $N(\varepsilon_F)$, and EPC constant λ for the two systems.

For CoN, the contraction of the lattice induces a relative decrease in the EPC constant, reduced to $\lambda = 0.18$ with a strain of −1%. Nevertheless, a moderate expansion of the lattice significantly enhances the EPC, with the λ jumping to a value of 1.2 and the resultant T_c reaching 7-12 K ($\mu^* = 0.2$-0.1) under a tensile strain of 2%. In sharp contrast, regardless of the applied strain, the λ of the CoP system remains almost unchanged or even decreases slightly, suggesting a constantly very low T_c. One reason for this contrast between the two systems originates from the vast difference in their electronic density of states at the Fermi level, since λ is proportional to $N(\varepsilon_F)$ when other parameters are kept unchanged [71]. As shown in Figure 3(i), the $N(\varepsilon_F)$ in the CoN system increases significantly with the tensile strain, which is equivalent to effective charge doping [72-74]. In contrast,

the $N(\varepsilon_F)$ in the CoP system remains almost constant. The detailed comparisons of the band structures and DOS for both systems under 0%, 2%, and 4% equi-biaxial strains are given in Figure S5.

To explore potential other reasons, we also analyze the lattice dynamics of the deformed systems, the evolution of the phonon spectra, and the associated EPC with increasing tensile strains. By comparing Figure 3(a), (c) and (e) for CoN, we find an overall spectral softening at increasing strain, reflecting a general weakening of the deformed Co–N bonds. In particular, there is a pronounced phonon softening accompanied by a large drop of the frequency (indicated by the green arrows in Figure 3(a), (c), and (e)), resulting in a remarkable increase in the EPC and a steep rise of $\lambda(\omega)$ in the corresponding low-frequency range. This point can be un-

derstood according to eq. (2). Since $\lambda_{qv} \propto \gamma_{qv}/\omega_{qv}^2$, given a sizable γ_{qv}, a further drop in the low-frequency part leads to small frequencies of the acoustic phonons, contributing substantially to the λ_{qv}'s, which account for 85% of the total λ, as shown in Figure 3(c). Moreover, when exerting a 4% tensile strain (Figure 3(e)), the frequencies of the acoustic modes turn to be negative, indicating that the system becomes unstable. In contrast, for CoP, the overall softening of the phonon spectra is very small (Figure 3(b), (d), and (f)), which explains that the EPC of the system remains basically unchanged. Here, the system is still stable when the tensile strain reaches 4%.

3.4   Magnetic properties

To explore the possibility of magnetic ordering in both two systems, we consider four magnetic configurations on Co atoms, namely, the nonmagnetic (NM), ferromagnetic (FM), Néel antiferromagnetic (NAFM), and collinear antiferromagnetic (CAFM) phases, as shown in Figure 4(a). Here, the on-site Hubbard U as an empirical parameter is further used to describe the correlation of the 3d electrons. The results for the CoN and CoP monolayers are presented in Figure 4(b) and (c), including the relative energies ΔE defined as $\Delta E = E - E_{NM}$, where E and E_{NM} are the total energies of a given magnetic and NM configurations, respectively, and the magnetic moments M in different magnetic configurations, both as functions of U. As a comparison, the corresponding results for a FeSe monolayer

are shown in Figure S6. We find that when U is increased to 2 and 5 eV for CoN and CoP, respectively, the ground states start to develop finite magnetic moment, which saturates at about 2 μ_B per Co at large enough U for both systems. In contrast, the ground state of FeSe is CAFM even at $U = 0$, and M varies within (2-4) μ_B per Fe when $U = 0$-6 eV. In addition, for a given U, the relative energies ΔE for CoN and CoP are much lower (by about an order of magnitude) than that for FeSe. Such distinct differences indicate that the CoN and CoP systems have a much weaker tendency toward developing magnetization compared with FeSe. It is noted that there is no experimental evidence for long-range magnetic ordering in either bulk or monolayered FeSe. Although magnetism can have a significant impact on the electronic structure and topological characteristics of the system, we expect that magnetism is very weak in the CoN and CoP systems and thereby mainly focus on their properties in the nonmagnetic case. Moreover, the difference in magnetism between the CoX and FeSe systems may also provide a crucial angle to elucidate the dominant microscopic mechanisms of superconductivity in these and related systems.

4   Discussion and conclusions

Based on proximity effects in reciprocal space, one of the three prevailing schemes to achieve TSC [11], when the Cooper pairs are introduced into the topological edge states, those edge states exhibit 1D TSC. For the CoN system, as
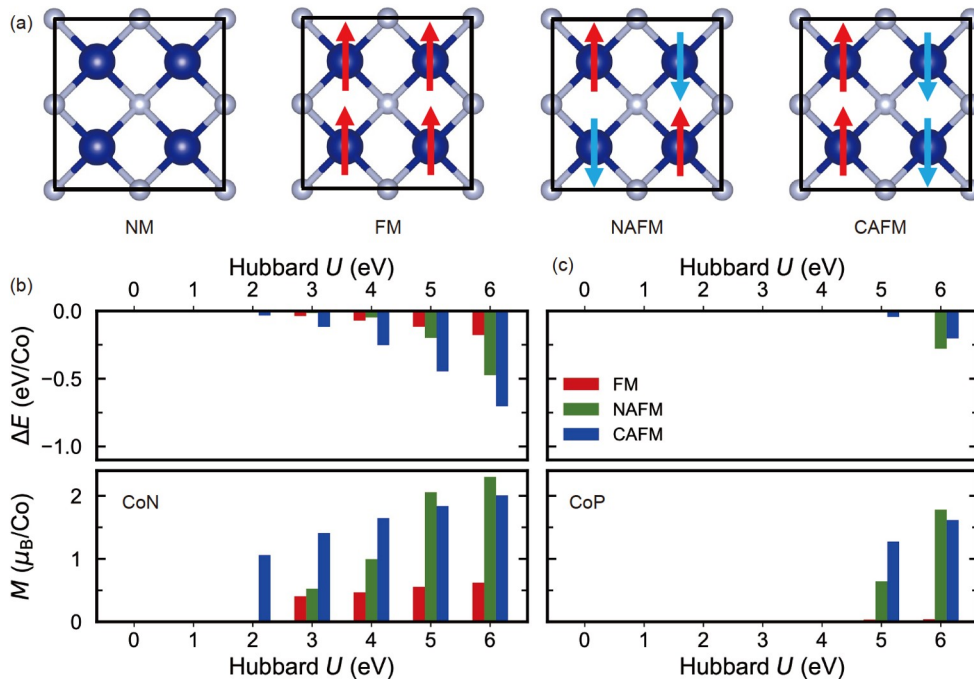

Figure 4   (Color online) (a) Four common magnetic configurations. (b), (c) Relative energy ΔE (upper panel) and magnetic moment M (lower panel) of the four magnetic configurations as functions of the on-site Hubbard U for CoN and CoP monolayers.

shown in Figure 2(e), the topological edge states are about 0.1 eV above the Fermi level, which can participate in the superconductivity under proper electron doping or gating of the samples. For the CoP system, as shown in Figure 2(f), the topological edge states cross the Fermi level along the $\overline{X} - \overline{\Gamma}$ path. Below the superconducting critical temperature, such topological edge states around the Fermi level can open a superconducting gap, which can make the edge states topologically superconducting. In addition, we also observe the existence of some other edge states whose dominant features characterize them as trivial in the two systems. When the superconducting electrons from the 2D bulk are only through these trivial edge states, the system is a superconductor but with no 1D TSC residing at the edges. As for experimentally resolving the topologically protected surface or edge states in the systems that are metallic, high-resolution angle-resolved photoemission spectroscopy (ARPES) measurements can reveal the spin-momentum-locking surface states, as demonstrated in FeTe$_{1-x}$Se$_x$ [75], and *in situ* scanning tunneling microscopy/spectroscopy (STM/STS) measurements can identify the enhanced intensity of local density states of the edges and their robustness, as demonstrated in some 2D systems [30,76-78].

Before closing, we briefly discuss the physically realistic growth aspects of the two systems. First, monolayered CoN or CoP with the tetragonal structure is expected to be grown on oxide substrates such as SrTiO$_3$ (STO) or other proper substrates by MBE, which is the most convenient way to grow such ultrathin materials. Given the three-atomic-layer structure (N-Co-N/P-Co-P) of the monolayers, it may be desirable to deposit N/P first, followed by proper amounts of Co and N/P. During growth, the deposition rates of the source atoms and the temperature need to be carefully controlled to avoid growing into the 3D bulk structure. Second, in order to maintain the topologically nontrivial properties of the two systems, the interaction with the substrates should not be too strong to affect their electronic structures, with van der Waals-type interactions preferred. Here, we also consider SrO$_2$ and STO as potential substrates for growing CoN and CoP, respectively, and investigate their band topology. As shown in Figures S7 and S8, both systems preserve the nontrivial band topology with the same topologicalization mechanism as that of their monolayer systems. Third, the substrates can introduce the strain effect due to the lattice mismatch. According to Figure 2(g) and (h), the two systems exhibit topologically nontrivial properties under a wide range of equi-biaxial strains, indicating their robustness against lattice deformation. As for superconductivity, the T_c of the CoN is significantly enhanced under equi-biaxial tensile strain, while the CoP always possesses very low T_c. Therefore, the tensile strains are favorable for the CoN system to harbor higher superconducting T_c. Due to extensive computational requirements, it is challenging to calculate the T_c of systems involving the substrates. Instead, we calculate $N(\varepsilon_F)$ to be 6.1 (7.7) and 6.5 (8.3) states/eV for freestanding strained CoN (CoP) and CoN/SrO$_2$ (CoP/STO), respectively, to examine the substrate effects while excluding the strain effect. The relatively small difference in $N(\varepsilon_F)$ implies that the superconducting properties of strained CoN (CoP) would be largely preserved when involving the SrO$_2$ (STO) substrate. Fourth, as demonstrated in the FeSe/STO systems [79-83], we also expect that charge carriers or some phonon modes from the substrates can transfer or penetrate into the overlayer to further enhance T_c. We have explored the charge doping effect of the substrate, which is simulated by adding electrons to or removing electrons from the CoN and CoP with a compensating uniform charge background of opposite signs. As shown in Figure S9, when doping 0.4 electrons per unit cell into the two systems, the EPC for the CoN is enhanced ($\lambda = 0.47$, $T_c = 1.97$ K, $\mu^* = 0.1$), while it is weakened for CoP, with the λ decreased to 0.12. Fifth, since the T_c of CoN can be significantly enhanced when applying a tensile strain, the experimental realization of such strains should be proposed. One way is to exert a tensile strain via proper substrates on which the CoN monolayer can grow, as already demonstrated in FeSe monolayers. For example, when the FeSe monolayer is grown on the Nb:SrTiO$_3$ or Nb:SrTiO$_3$/KTaO$_3$ substrate, the in-plane lattice constant can expand to 3.90 or 3.99 Å, suggesting a 3.7% or 6.1% tensile strain [68,84]. The tensile strain can also be applied to the thin films by bending a flexible substrate, as reported in monolayer and bilayer MoS$_2$ where 0-2.2% strains have been achieved [85]. Finally, the growth and realization of the superconductivity of the two systems are also encouraged by the recent experimental progress on the CoSb monolayers. The CoSb films in an orthogonal phase have been fabricated on STO, and a symmetric gap around the Fermi level with coherence peaks at 7 meV as well as a diamagnetic transition at 14 K has been observed, suggesting the emergence of superconductivity [58]. Further, beyond the superconducting properties, CoSb$_{1-x}$ nanoribbons with quasi-one-dimensional stripes have been fabricated on STO, exhibiting signatures of the Tomonaga-Luttinger liquid state [86].

To summarize, by employing first-principles approaches and following the isovalency rule, we have predicted monolayered CoN and CoP to be energetically stable, and have systematically investigated their electronic, topological, and superconducting properties. Our calculations have identified that both monolayers are dynamically and thermodynamically stable when adopting the monolayered FeSe structure, even though none of them is a layered material in bulk form. Furthermore, the two systems have been shown to possess topologically nontrivial band properties, which originate from the joint effects of the intrinsic band inversion induced by crystal field splitting and SOC, characterized by both the odd Z_2 invariant and topologically protected edge

states. The mechanism of topologicalization is similar to the KM model, in contrast to the CoX (X = As, Sb, Bi) systems where the SOC has a dual function of inducing the band inversion and causing nontrivial band topology, as in the BHZ model. Intriguingly, under equi-biaxial tensile strains, the two systems have completely different behaviors on superconductivity. The EPC strength of monolayered CoN is abruptly enhanced and reaches a maximum value of 1.2 with increasing strain, yielding T_c of 7-12 K ($\mu^* = 0.2$-0.1), while the EPC strength of the CoP monolayer almost stays intact under strain. The underlying reasons are the increased electronic density of states near the Fermi level and significant phonon softening in CoN upon pressuring. Collectively, the present study further enriches our understanding of different mechanisms of band inversions and topologicalization, and also offers highly appealing platforms for exploiting the coexistence of and interaction between the superconducting state and topologically protected edge states in the 2D limit.

Conflict of interest The authors declare that they have no conflict of interest.

Supporting Information

The supporting information is available online at http://phys.scichina.com and https://link.springer.com. The supporting materials are published as submitted, without typesetting or editing. The responsibility for scientific accuracy and content remains entirely with the authors.

1 Y. Saito, T. Nojima, and Y. Iwasa, Nat. Rev. Mater. **2**, 16094 (2017).
2 N. Reyren, S. Thiel, A. D. Caviglia, L. F. Kourkoutis, G. Hammerl, C. Richter, C. W. Schneider, T. Kopp, A. S. Ruetschi, D. Jaccard, M. Gabay, D. A. Muller, J. M. Triscone, and J. Mannhart, Science **317**, 1196 (2007).
3 A. Gozar, G. Logvenov, L. F. Kourkoutis, A. T. Bollinger, L. A. Giannuzzi, D. A. Muller, and I. Bozovic, Nature **455**, 782 (2008).
4 S. Qin, J. Kim, Q. Niu, and C. K. Shih, Science **324**, 1314 (2009).
5 T. Zhang, P. Cheng, W. J. Li, Y. J. Sun, G. Wang, X. G. Zhu, K. He, L. Wang, X. Ma, X. Chen, Y. Wang, Y. Liu, H. Q. Lin, J. F. Jia, and Q. K. Xue, Nat. Phys. **6**, 104 (2010).
6 J. T. Ye, S. Inoue, K. Kobayashi, Y. Kasahara, H. T. Yuan, H. Shimotani, and Y. Iwasa, Nat. Mater. **9**, 125 (2010).
7 J. T. Ye, Y. J. Zhang, R. Akashi, M. S. Bahramy, R. Arita, and Y. Iwasa, Science **338**, 1193 (2012).
8 Y. Yu, L. Ma, P. Cai, R. Zhong, C. Ye, J. Shen, G. D. Gu, X. H. Chen, and Y. Zhang, Nature **575**, 156 (2019).
9 Q. Y. Wang, Z. Li, W. H. Zhang, Z. C. Zhang, J. S. Zhang, W. Li, H. Ding, Y. B. Ou, P. Deng, K. Chang, J. Wen, C. L. Song, K. He, J. F. Jia, S. H. Ji, Y. Y. Wang, L. L. Wang, X. Chen, X. C. Ma, and Q. K. Xue, Chin. Phys. Lett. **29**, 037402 (2012).
10 C. W. J. Beenakker, Annu. Rev. Condens. Matter Phys. **4**, 113 (2013).
11 W. Qin, J. Gao, P. Cui, and Z. Zhang, Sci. China-Phys. Mech. Astron. **66**, 267005 (2023).
12 W. Qin, L. Li, and Z. Zhang, Nat. Phys. **15**, 796 (2019).
13 Y. Cao, V. Fatemi, S. Fang, K. Watanabe, T. Taniguchi, E. Kaxiras, and P. Jarillo-Herrero, Nature **556**, 43 (2018).
14 W. Qin, and A. H. MacDonald, Phys. Rev. Lett. **127**, 097001 (2021).
15 H. Zhou, T. Xie, T. Taniguchi, K. Watanabe, and A. F. Young, Nature **598**, 434 (2021).
16 H. Zhou, L. Holleis, Y. Saito, L. Cohen, W. Huynh, C. L. Patterson, F. Yang, T. Taniguchi, K. Watanabe, and A. F. Young, Science **375**, 774 (2022).
17 N. F. Q. Yuan, K. F. Mak, and K. T. Law, Phys. Rev. Lett. **113**, 097001 (2014).
18 N. Hao, and J. Hu, Phys. Rev. X **4**, 031053 (2014).
19 Z. F. Wang, H. Zhang, D. Liu, C. Liu, C. Tang, C. Song, Y. Zhong, J. Peng, F. Li, C. Nie, L. Wang, X. J. Zhou, X. Ma, Q. K. Xue, and F. Liu, Nat. Mater. **15**, 968 (2016).
20 X. Shi, Z. Q. Han, P. Richard, X. X. Wu, X. L. Peng, T. Qian, S. C. Wang, J. P. Hu, Y. J. Sun, and H. Ding, Sci. Bull. **62**, 503 (2017).
21 C. Liu, C. Chen, X. Liu, Z. Wang, Y. Liu, S. Ye, Z. Wang, J. Hu, and J. Wang, Sci. Adv. **6**, eaax7547 (2020).
22 Z. Fei, T. Palomaki, S. Wu, W. Zhao, X. Cai, B. Sun, P. Nguyen, J. Finney, X. Xu, and D. H. Cobden, Nat. Phys. **13**, 677 (2017).
23 S. Tang, C. Zhang, D. Wong, Z. Pedramrazi, H. Z. Tsai, C. Jia, B. Moritz, M. Claassen, H. Ryu, S. Kahn, J. Jiang, H. Yan, M. Hashimoto, D. Lu, R. G. Moore, C. C. Hwang, C. Hwang, Z. Hussain, Y. Chen, M. M. Ugeda, Z. Liu, X. Xie, T. P. Devereaux, M. F. Crommie, S. K. Mo, and Z. X. Shen, Nat. Phys. **13**, 683 (2017).
24 E. Sajadi, T. Palomaki, Z. Fei, W. Zhao, P. Bement, C. Olsen, S. Luescher, X. Xu, J. A. Folk, and D. H. Cobden, Science **362**, 922 (2018).
25 V. Fatemi, S. Wu, Y. Cao, L. Bretheau, Q. D. Gibson, K. Watanabe, T. Taniguchi, R. J. Cava, and P. Jarillo-Herrero, Science **362**, 926 (2018).
26 C. Liu, C. S. Lian, M. H. Liao, Y. Wang, Y. Zhong, C. Ding, W. Li, C. L. Song, K. He, X. C. Ma, W. Duan, D. Zhang, Y. Xu, L. Wang, and Q. K. Xue, Phys. Rev. Mater. **2**, 094001 (2018).
27 J. Chen, and Y. Ge, Phys. Rev. B **103**, 064510 (2021).
28 D. Campi, S. Kumari, and N. Marzari, Nano Lett. **21**, 3435 (2021).
29 J. Gao, W. Ding, S. Zhang, Z. Zhang, and P. Cui, Nano Lett. **21**, 7396 (2021).
30 C. Zhao, L. Li, L. Zhang, J. Qin, H. Chen, B. Xia, B. Yang, H. Zheng, S. Wang, C. Liu, Y. Li, D. Guan, P. Cui, Z. Zhang, and J. Jia, Phys. Rev. Lett. **128**, 206802 (2022).
31 B. A. Bernevig, T. L. Hughes, and S. C. Zhang, Science **314**, 1757 (2006).
32 C. L. Kane, and E. J. Mele, Phys. Rev. Lett. **95**, 226801 (2005).
33 G. Kresse, and J. Furthmüller, Phys. Rev. B **54**, 11169 (1996).
34 G. Kresse, and D. Joubert, Phys. Rev. B **59**, 1758 (1999).
35 J. P. Perdew, K. Burke, and M. Ernzerhof, Phys. Rev. Lett. **77**, 3865 (1996).
36 S. Nosé, J. Chem. Phys. **81**, 511 (1984).
37 W. G. Hoover, Phys. Rev. A **31**, 1695 (1985).
38 A. A. Soluyanov, and D. Vanderbilt, Phys. Rev. B **83**, 235401 (2011).
39 M. P. L. Sancho, J. M. Lopez Sancho, J. M. L. Sancho, and J. Rubio, J. Phys. F-Met. Phys. **15**, 851 (1985).
40 A. A. Mostofi, J. R. Yates, Y. S. Lee, I. Souza, D. Vanderbilt, and N. Marzari, Comput. Phys. Commun. **178**, 685 (2008).
41 G. Pizzi, V. Vitale, R. Arita, S. Blügel, F. Freimuth, G. Géranton, M. Gibertini, D. Gresch, C. Johnson, T. Koretsune, J. Ibañez-Azpiroz, H. Lee, J. M. Lihm, D. Marchand, A. Marrazzo, Y. Mokrousov, J. I. Mustafa, Y. Nohara, Y. Nomura, L. Paulatto, S. Poncé, T. Ponweiser, J. Qiao, F. Thöle, S. S. Tsirkin, M. Wierzbowska, N. Marzari, D. Vanderbilt, I. Souza, A. A. Mostofi, and J. R. Yates, J. Phys.-Condens. Matter **32**, 165902 (2020).
42 Q. S. Wu, S. N. Zhang, H. F. Song, M. Troyer, and A. A. Soluyanov, Comput. Phys. Commun. **224**, 405 (2018).
43 S. Poncé, E. R. Margine, C. Verdi, and F. Giustino, Comput. Phys. Commun. **209**, 116 (2016).
44 P. Giannozzi, S. Baroni, N. Bonini, M. Calandra, R. Car, C. Ca-

vazzoni, D. Ceresoli, G. L. Chiarotti, M. Cococcioni, I. Dabo, A. Dal Corso, S. de Gironcoli, S. Fabris, G. Fratesi, R. Gebauer, U. Gerstmann, C. Gougoussis, A. Kokalj, M. Lazzeri, L. Martin-Samos, N. Marzari, F. Mauri, R. Mazzarello, S. Paolini, A. Pasquarello, L. Paulatto, C. Sbraccia, S. Scandolo, G. Sclauzero, A. P. Seitsonen, A. Smogunov, P. Umari, and R. M. Wentzcovitch, J. Phys.-Condens. Matter **21**, 395502 (2009).

45 M. J. van Setten, M. Giantomassi, E. Bousquet, M. J. Verstraete, D. R. Hamann, X. Gonze, and G. M. Rignanese, Comput. Phys. Commun. **226**, 39 (2018).

46 W. L. McMillan, Phys. Rev. **167**, 331 (1968).

47 P. B. Allen, and R. C. Dynes, Phys. Rev. B **12**, 905 (1975).

48 F. Giustino, Rev. Mod. Phys. **89**, 015003 (2017).

49 N. Mounet, M. Gibertini, P. Schwaller, D. Campi, A. Merkys, A. Marrazzo, T. Sohier, I. E. Castelli, A. Cepellotti, G. Pizzi, and N. Marzari, Nat. Nanotech. **13**, 246 (2018).

50 Z. Zhu, X. Cai, S. Yi, J. Chen, Y. Dai, C. Niu, Z. Guo, M. Xie, F. Liu, J. H. Cho, Y. Jia, and Z. Zhang, Phys. Rev. Lett. **119**, 106101 (2017).

51 M. C. Lucking, W. Xie, D. H. Choe, D. West, T. M. Lu, and S. B. Zhang, Phys. Rev. Lett. **120**, 086101 (2018).

52 W. Ding, J. Zeng, W. Qin, P. Cui, and Z. Zhang, Phys. Rev. Lett. **124**, 027002 (2020).

53 X. Huang, J. Guan, Z. Lin, B. Liu, S. Xing, W. Wang, and J. Guo, Nano Lett. **17**, 4619 (2017).

54 Y. Wang, G. Qiu, R. Wang, S. Huang, Q. Wang, Y. Liu, Y. Du, W. A. Goddard III, M. J. Kim, X. Xu, P. D. Ye, and W. Wu, Nat. Electron. **1**, 228 (2018).

55 S. Berweger, G. Qiu, Y. Wang, B. Pollard, K. L. Genter, R. Tyrrell-Ead, T. M. Wallis, W. Wu, P. D. Ye, and P. Kabos, Nano Lett. **19**, 1289 (2019).

56 X. Lin, J. C. Lu, Y. Shao, Y. Y. Zhang, X. Wu, J. B. Pan, L. Gao, S. Y. Zhu, K. Qian, Y. F. Zhang, D. L. Bao, L. F. Li, Y. Q. Wang, Z. L. Liu, J. T. Sun, T. Lei, C. Liu, J. O. Wang, K. Ibrahim, D. N. Leonard, W. Zhou, H. M. Guo, Y. L. Wang, S. X. Du, S. T. Pantelides, and H. J. Gao, Nat. Mater. **16**, 717 (2017).

57 L. Gao, J. T. Sun, J. C. Lu, H. Li, K. Qian, S. Zhang, Y. Y. Zhang, T. Qian, H. Ding, X. Lin, S. Du, and H. J. Gao, Adv. Mater. **30**, 1707055 (2018).

58 C. Ding, G. Gong, Y. Liu, F. Zheng, Z. Zhang, H. Yang, Z. Li, Y. Xing, J. Ge, K. He, W. Li, P. Zhang, J. Wang, L. Wang, and Q. K. Xue, ACS Nano **13**, 10434 (2019).

59 L. Qin, Z. H. Zhang, Z. Jiang, K. Fan, W. H. Zhang, Q. Y. Tang, H. N. Xia, F. Meng, Q. Zhang, L. Gu, D. West, S. Zhang, and Y. S. Fu, ACS Nano **15**, 8184 (2021).

60 K. Mustonen, C. Hofer, P. Kotrusz, A. Markevich, M. Hulman, C. Mangler, T. Susi, T. J. Pennycook, K. Hricovini, C. Richter, J. C. Meyer, J. Kotakoski, and V. Skákalová, Adv. Mater. **34**, 2106922 (2022).

61 Z. Wang, P. Zhang, G. Xu, L. K. Zeng, H. Miao, X. Xu, T. Qian, H. Weng, P. Richard, A. V. Fedorov, H. Ding, X. Dai, and Z. Fang, Phys. Rev. B **92**, 115119 (2015).

62 Y. Xu, B. Yan, H. J. Zhang, J. Wang, G. Xu, P. Tang, W. Duan, and S. C. Zhang, Phys. Rev. Lett. **111**, 136804 (2013).

63 X. Qian, J. Liu, L. Fu, and J. Li, Science **346**, 1344 (2014).

64 H. Weng, A. Ranjbar, Y. Liang, Z. Song, M. Khazaei, S. Yunoki, M. Arai, Y. Kawazoe, Z. Fang, and X. Dai, Phys. Rev. B **92**, 075436

65 Y. Ma, L. Kou, X. Li, Y. Dai, S. C. Smith, and T. Heine, Phys. Rev. B **92**, 085427 (2015).

66 C. Si, K. H. Jin, J. Zhou, Z. Sun, and F. Liu, Nano Lett. **16**, 6584 (2016).

67 T. Wei, and Z. Zhang, Phys. Rev. B **104**, 184503 (2021).

68 R. Peng, H. C. Xu, S. Y. Tan, H. Y. Cao, M. Xia, X. P. Shen, Z. C. Huang, C. H. P. Wen, Q. Song, T. Zhang, B. P. Xie, X. G. Gong, and D. L. Feng, Nat. Commun. **5**, 5044 (2014).

69 S. Zeng, Y. Zhao, G. Li, and J. Ni, Phys. Rev. B **94**, 024501 (2016).

70 Y. Song, Z. Chen, Q. Zhang, H. Xu, X. Lou, X. Chen, X. Xu, X. Zhu, R. Tao, T. Yu, H. Ru, Y. Wang, T. Zhang, J. Guo, L. Gu, Y. Xie, R. Peng, and D. Feng, Nat. Commun. **12**, 5926 (2021).

71 G. Profeta, M. Calandra, and F. Mauri, Nat. Phys. **8**, 131 (2012).

72 S. He, J. He, W. Zhang, L. Zhao, D. Liu, X. Liu, D. Mou, Y. B. Ou, Q. Y. Wang, Z. Li, L. Wang, Y. Peng, Y. Liu, C. Chen, L. Yu, G. Liu, X. Dong, J. Zhang, C. Chen, Z. Xu, X. Chen, X. Ma, Q. Xue, and X. J. Zhou, Nat. Mater. **12**, 605 (2013).

73 J. Shiogai, Y. Ito, T. Mitsuhashi, T. Nojima, and A. Tsukazaki, Nat. Phys. **12**, 42 (2015).

74 B. Lei, J. H. Cui, Z. J. Xiang, C. Shang, N. Z. Wang, G. J. Ye, X. G. Luo, T. Wu, Z. Sun, and X. H. Chen, Phys. Rev. Lett. **116**, 077002 (2016).

75 P. Zhang, K. Yaji, T. Hashimoto, Y. Ota, T. Kondo, K. Okazaki, Z. Wang, J. Wen, G. D. Gu, H. Ding, and S. Shin, Science **360**, 182 (2018).

76 F. Yang, L. Miao, Z. F. Wang, M. Y. Yao, F. Zhu, Y. R. Song, M. X. Wang, J. P. Xu, A. V. Fedorov, Z. Sun, G. B. Zhang, C. Liu, F. Liu, D. Qian, C. L. Gao, and J. F. Jia, Phys. Rev. Lett. **109**, 016801 (2012).

77 I. K. Drozdov, A. Alexandradinata, S. Jeon, S. Nadj-Perge, H. Ji, R. J. Cava, B. Andrei Bernevig, and A. Yazdani, Nat. Phys. **10**, 664 (2014).

78 S. Kezilebieke, M. N. Huda, V. Vaňo, M. Aapro, S. C. Ganguli, O. J. Silveira, S. Głodzik, A. S. Foster, T. Ojanen, and P. Liljeroth, Nature **588**, 424 (2020).

79 W. Zhang, Z. Li, F. Li, H. Zhang, J. Peng, C. Tang, Q. Wang, K. He, X. Chen, L. Wang, X. Ma, and Q. K. Xue, Phys. Rev. B **89**, 060506 (2014).

80 J. J. Lee, F. T. Schmitt, R. G. Moore, S. Johnston, Y. T. Cui, W. Li, M. Yi, Z. K. Liu, M. Hashimoto, Y. Zhang, D. H. Lu, T. P. Devereaux, D. H. Lee, and Z. X. Shen, Nature **515**, 245 (2014).

81 S. Zhang, J. Guan, X. Jia, B. Liu, W. Wang, F. Li, L. Wang, X. Ma, Q. Xue, J. Zhang, E. W. Plummer, X. Zhu, and J. Guo, Phys. Rev. B **94**, 081116 (2016).

82 H. Zhang, D. Zhang, X. Lu, C. Liu, G. Zhou, X. Ma, L. Wang, P. Jiang, Q. K. Xue, and X. Bao, Nat. Commun. **8**, 214 (2017).

83 S. Zhang, T. Wei, J. Guan, Q. Zhu, W. Qin, W. Wang, J. Zhang, E. W. Plummer, X. Zhu, Z. Zhang, and J. Guo, Phys. Rev. Lett. **122**, 066802 (2019).

84 S. Tan, Y. Zhang, M. Xia, Z. Ye, F. Chen, X. Xie, R. Peng, D. Xu, Q. Fan, H. Xu, J. Jiang, T. Zhang, X. Lai, T. Xiang, J. Hu, B. Xie, and D. Feng, Nat. Mater. **12**, 634 (2013).

85 H. J. Conley, B. Wang, J. I. Ziegler, R. F. Haglund Jr., S. T. Pantelides, and K. I. Bolotin, Nano Lett. **13**, 3626 (2013).

86 R. Lou, M. Lei, W. Ding, W. Yang, X. Chen, R. Tao, S. Ding, X. Shen, Y. Yan, P. Cui, H. Xu, R. Peng, T. Zhang, Z. Zhang, and D. Feng, npj Quantum Mater. **6**, 79 (2021).